ACS OMEGA

Article

Cite This: ACS Omega 2019, 4, 18495−18501

http://pubs.acs.org/journal/acsodf

New Synthetic Route for the Growth of α-FeOOH/NH_2-Mil-101 Films on Copper Foil for High Surface Area Electrodes

Francesca Monforte,[†,‡] Mario Urso,[§] Alessandra Alberti,[‡] Emanuele Smecca,[‡] Salvo Mirabella,[§] Corrado Bongiorno,[‡] Giovanni Mannino,[‡] and Guglielmo Guido Condorelli*[,†]

[†]Dipartimento di Scienze Chimiche, Università degli Studi di Catania and INSTM UdR di Catania, Viale Andrea Doria 6, Catania 95125, Italy

[‡]CNR-IMM, Strada VIII no. 5 Zona Industriale, Catania 95121, Italy

[§]Dipartimento di Fisica e Astronomia, Università degli Studi di Catania, Via S. Sofia 64, Catania 95123, Italy

ABSTRACT: A novel metal organic framework (MOF)-based composite was synthesized on a Cu substrate via a two-step route. An amorphous iron oxide/hydroxide layer was first deposited on a Cu foil through a sol−gel process; then, Fe-NH_2-Mil-101 was grown using both the iron oxide/hydroxide matrix, which provided the Fe^{3+} centers needed for MOF formation, and 2-amino-terephthalic acid ethanol solution. This innovative synthetic strategy is a convenient approach to grow metal oxide/hydroxide and MOF composite films. Structural, chemical, and morphological characterizations suggest that the obtained composite is made up of both the α-FeOOH goethite and the NH_2-Mil-101 phases featuring a hybrid heterostructure. The electrochemical features of the composite structure were investigated using electrochemical impedance spectroscopy. The impedance behavior of the α-FeOOH/NH_2-Mil-101 films indicates that they can be used as efficient high surface area metal hydroxide/MOF-based electrodes for applications such as energy storage and sensing.

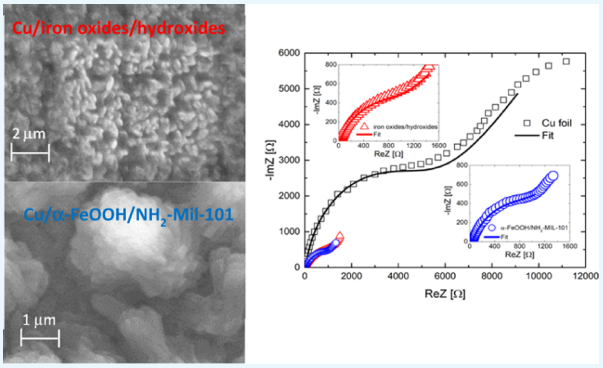

INTRODUCTION

Metal organic framework (MOF)-based hybrid composites are promising platforms for the development of innovative electrochemical systems such as supercapacitors, batteries, and sensors.[1−4] The combination of individual components in a common matrix makes it possible to optimize specific chemical−physical properties guaranteeing multifunctionality and versatility of the composite.[5,6] In particular, MOF/metal oxide (MO) hybrid materials have been researched with the aim of developing next-generation electrodes for lithium and/or sodium batteries and for photo-electrochemical water splitting devices.[7−10] In these systems, MOFs offer flexible coordination networks characterized by high surface areas, low densities, and tunable pore sizes.[11−13] Additionally, appropriate functionalities can be added to the MOF organic building blocks through postsynthetic modifications in order to modulate MOF properties.[14,15] Despite their advantages, pure MOFs are not usually used for electrochemical applications because of their poor chemical stability and low electrical conductivity, which reduce their energy storage capabilities.[3,16] For this reason, MOFs are usually used as precursors of composite carbon−MO electrodes as they can be converted, through thermal annealing, into MO nanoparticles and into porous carbon networks.[17−19] In particular, transition MOs (such as Fe_2O_3, CoO, Cu_2O, RuO_2, and TiO_2), are efficient active electrodes capable of performing reversible conversion reactions guaranteeing accurate redox potential control.[20−22] In addition, the hybrid nanostructures of the MOs embedded in a carbon matrix improve the electrochemical performances compared to those of pure oxides because of short-ion diffusion and their increased conductivity.[23,24] Among the various transition MOs, iron oxides have been widely employed as anode materials because of them being environmentally friendly and characterized by high theoretical capacity, high corrosion resistance, and wide working potential ranges.[25,26] Several iron oxide and hydroxide systems have been developed with different morphologies, porosities, and crystalline degrees.[27−29] Amorphous or low crystalline iron oxide or FeOOH porous materials can be used as highly efficient electrodes, especially if defect sites increasing ion mobility and improving electrolyte diffusion are inserted into the crystal lattice.[30−32]

The most common synthetic methods to achieve iron oxide-based electrodes are sol−gel routes and MOF pyrolysis.[33,34] In particular, Fe-Mil-88 and Fe-Mil-101 are the MOF precursors usually used for pyrolysis.[35,36] These precursors collapse after pyrolysis, shaping conductive mesoporous carbon shells around the iron oxide core, thus overcoming the problem of

Received: June 20, 2019
Accepted: October 10, 2019
Published: November 1, 2019

DOI: 10.1021/acsomega.9b01840
ACS Omega 2019, 4, 18495−18501

the low conductivity of the MOF coating.[37] On the other hand, it is important to develop synthetic routes that, unlike previous methods,[35,36] do not require high temperatures to obtain low-impedance hybrid composite films consisting of transition MOs coated with undecomposed MOFs. In fact, this approach could lead to new and efficient electrode materials capable of exploiting the structural versatility and high surface area of MOFs. To this aim, it is important to understand the effects of surface chemistry and synthetic conditions on the direct growth of MOFs on the electrode surface[38,39] and to evaluate how the obtained coating affects the electrochemical properties. For this reason, in this study, we describe the growth of a novel MOF-based hybrid film on a copper foil, consisting of Fe-NH_2-Mil-101 embedded in α-FeOOH matrix. The adopted synthesis is made up of two reaction steps: the first is the sol–gel deposition of amorphous iron oxides/hydroxides; the second is the direct growth of Fe-NH_2-Mil-101 on the iron oxide/hydroxide film using a solution containing the MOF organic building block only, namely, 2-aminoterephthalate acid. Electrochemical impedance spectroscopy (EIS) showed promising electrochemical features for the α-FeOOH/NH_2-Mil-101 hybrid system in terms of charge transfer resistance, capacitance, and diffusion resistance.

RESULTS AND DISCUSSION

Characterization of the α-FeOOH/NH_2-Mil-101 Composite. Figure 1 shows the field emission scanning electron microscopy (FE-SEM) images of the sol–gel deposited amorphous layer (Figure 1a) and of the α-FeOOH/NH_2-Mil-101 composite (Figure 1b,c) obtained through a 4 h MOF-growth process. Figure 1d shows the morphology of the bare copper foil. The sol–gel deposited iron oxide/hydroxide film is a homogenous and continuous layer characterized by a "bunch" morphology, typical of iron oxide materials (Figure 1a). NH_2-Mil-101 growth into the amorphous matrix increases the layer porosity (Figure 1b) through the formation of agglomerated clusters of rod-like crystals (Figure 1c), the typical shape of crystalline α-FeOOH (goethite). Note that the films obtained through an 8 h MOF-growth process led to a poor substrate coverage, likely because long reaction times determine too much FeOOH consumption, which reduces the adhesion between the copper substrate and the MOF crystals, thus favoring MOF crystal dispersion in the ethanol solution.

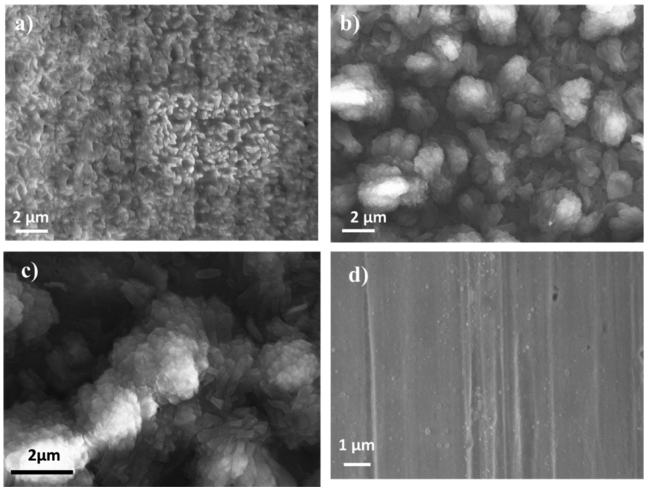

Figure 1. FE-SEM images of (a) iron oxide/hydroxide layer deposited via sol–gel on a Cu foil, (b) low and (c) high-magnification SEM images of the α-FeOOH/NH_2-Mil-101 composite; and (d) bare Cu foil surface.

To understand the nature of the features observed in the FE-SEM images, energy dispersive X-ray (EDX) mapping of the characteristic elements was also performed. Figure 2 compares the morphological images of FeOOH/NH_2-Mil-101 films (Figure 2a) with the distribution of carbon, iron, and copper (Figure 2b,c,–d, respectively).

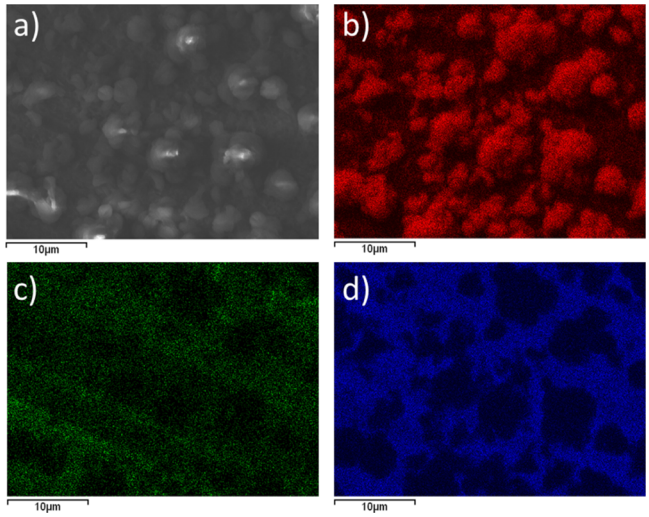

Figure 2. Morphological FE-SEM image (a) and EDX mapping (b–d) of the intensity of C Kα (b), Fe Kα (c), and Cu Kα (d) signals of the α-FeOOH/NH_2-Mil-101 composite.

From Figure 2, it is evident that the higher carbon signal corresponds to the agglomerated structures, suggesting that they contain carbon-rich species such as NH_2-Mil-101 crystals. As expected, in these regions, the intensity of the copper signal is low because of the agglomerated structures covering the substrate. The iron signal is present throughout the analyzed area, but its intensity is lower in the areas corresponding to the agglomerates. All these observations suggest that the agglomerated structures are rich in MOF crystals, whose main component is carbon and in which the density of iron atoms is lower than that of the FeOOH ones. The areas without the MOF-based structures, which show a lower carbon concentration, are mainly constituted of the unreacted iron oxide film.

The lattice structure of the obtained films was investigated by X-ray diffraction (XRD) measurements. The XRD pattern of the sol–gel FeOOH layer does not show any peak except for the two peaks at 2θ = 43.3° and 2θ = 50.4° related to the Cu substrate. According to the low temperature used for the postdeposition annealing (150 °C), this finding implies that the layer is amorphous. On the other hand, after the NH_2-Mil-101 growth, new features are observed in the diffraction pattern (Figure 3). In particular, in the range 2θ = 5–7°, a convolution of several contributions can be assigned to the Mil-101 film, related to (333), (511), and (531) crystallographic planes. In addition, a weak and noisy signal at $2\theta \approx 17°$ is found and can be attributed to (222) and (422) planes of the same structure (Mil-101).[40,41] We notice that, unlike the measurement on powders, specific features are not visible in the 2θ range between 2° and 5° because of the low amount of material, the copper foil roughness, and the high background

DOI: 10.1021/acsomega.9b01840
ACS Omega 2019, 4, 18495–18501

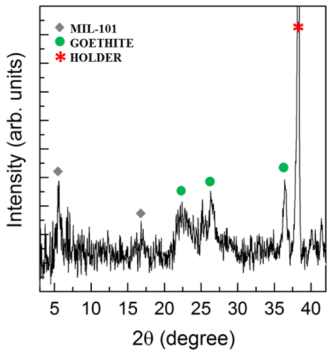

Figure 3. XRD diffractogram of the α-FeOOH/NH_2-Mil-101 composite.

caused by the reflection at grazing angles. As additional contributions, the peaks at $2\theta = 22.2°$, 26.4°, and 36.4° can be assigned to the (110), (021), and (111) planes of crystalline α-FeOOH (goethite), respectively, likely formed during the growth of the NH_2-Mil-101 film.[42]

Further information on the nature of the obtained composite was obtained through scanning transmission electron microscopy (STEM)/transmission electron microscopy (TEM) analyses performed upon scratching a portion of the sample on the TEM grid. Low- and high-magnification STEM images reported in Figure 4a,b show the contrast

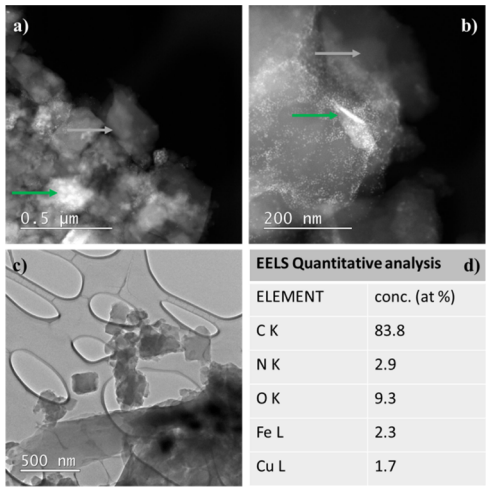

Figure 4. (a) Low- and (b) high-magnification STEM images in the dark field and (c) TEM image in the bright field of the α-FeOOH/NH_2-Mil-101 composite scratched of a Cu-lacey-C grid. Green and gray arrows indicate bright and dark areas, respectively; (d) estimated sample composition from EELS measurements.

difference between the dark and bright zones suggesting the presence of different density components. The darker zones (gray arrow), characterized by faceted contours, indicate the presence of a lower density component and are, therefore, attributable to the MOF matrix. The brighter areas (green arrow), which have less-defined shapes are because of the higher density component probably related to iron oxide. The TEM morphology in Figure 4c shows, in addition to the agglomerated small grains, the presence of well-defined isolated squared crystals of about 200 nm-size each. The sample composition (Figure 4d) was assessed through electron energy loss spectroscopy (EELS) measurements. The presence of similar amounts of Fe and N is consistent with the NH_2-Mil-101 molecular formula.

Complementary information on the nature of the α-FeOOH/NH_2-Mil-101 film was obtained by Fourier-transform infrared spectroscopy (FTIR). Figure 5 shows the spectra of

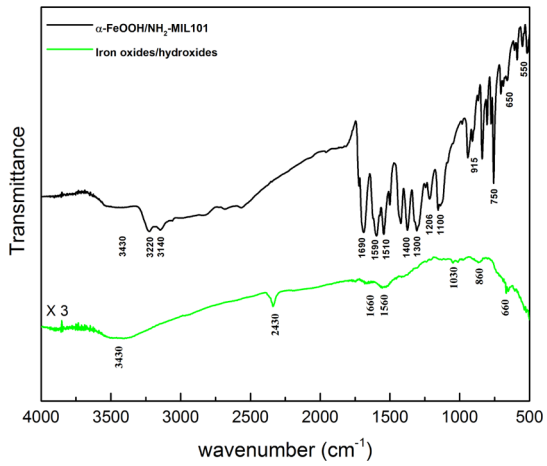

Figure 5. FTIR spectrum of the amorphous FeOOH layer (green) deposited via sol−gel on a Cu foil and the α-FeOOH/NH_2-Mil-101 composite (dark).

the sol−gel deposited film (green) and the α-FeOOH/NH_2-Mil-101 composite (dark). The spectrum of the sol−gel layer is consistent with the presence of iron oxides/hydroxides. The most intense signal is the broad band at 3430 cm^{-1} assigned to the −OH stretching vibrations of iron hydroxides and adsorbed water.[42] Signals at 860 and at 660 cm^{-1} are because of the Fe−O stretching modes typical of iron oxides and hydroxides.[42] The sharp peak at 2430 cm^{-1} is likely because of CO_3^{2-}, which is typically formed by the reaction of FeOOH with atmospheric CO_2,[43] whereas the peaks in the 1660−1560 cm^{-1} region are because of the −OH bending vibrations.[42,44] Note that, as expected for inorganic compounds, oxide/hydroxide signals are much weaker than the MOF ones. In fact, the IR spectrum of the α-FeOOH/NH_2-Mil-101 film shows much stronger signals, mainly due to the terephthalate ligand. In particular, the signals at 1590−1510 and at 1300−1400 cm^{-1} are typical of the COO^- asymmetric and symmetric stretchings of the terphthalate ligands.[41,45,46] However, the presence of unreacted terephthalic acid molecules is also detected through the signal at 1690 cm^{-1}.[45,47] The doublet at 3220 and 3140 cm^{-1} is assigned to the N−H asymmetric and symmetric stretches of the amino group. In addition, in the 1700−1100 cm^{-1} region, the signals due to the C−C and C−N deformation vibrations of the aminoterephthalic acid aromatic ring are also present.[41] Finally, the weak and broad shoulder at 3430 cm^{-1} can be associated to the −OH stretching of FeOOH and adsorbed water.

Information on the chemical nature of the composite surface was obtained through X-ray photoelectron spectroscopy (XPS). Figure 6 shows the high resolution XPS spectral region of the composite components: Fe $2p_{3/2}$, O 1s, C 1s, O 1s, and N 1s. The Fe $2p_{3/2}$ signal (Figure 6a) consists of two main components at 709.0 and 711.4 eV indicating the presence of Fe^{2+} and Fe^{3+}, respectively.[47,48] A third low band is because of the Fe^{2+} shake-up at about 715 eV. The Fe^{3+} component can be because of both the α-FeOOH and NH_2-Mil-101 phases, while the Fe^{2+} component is likely because of

DOI: 10.1021/acsomega.9b01840
ACS Omega 2019, 4, 18495−18501

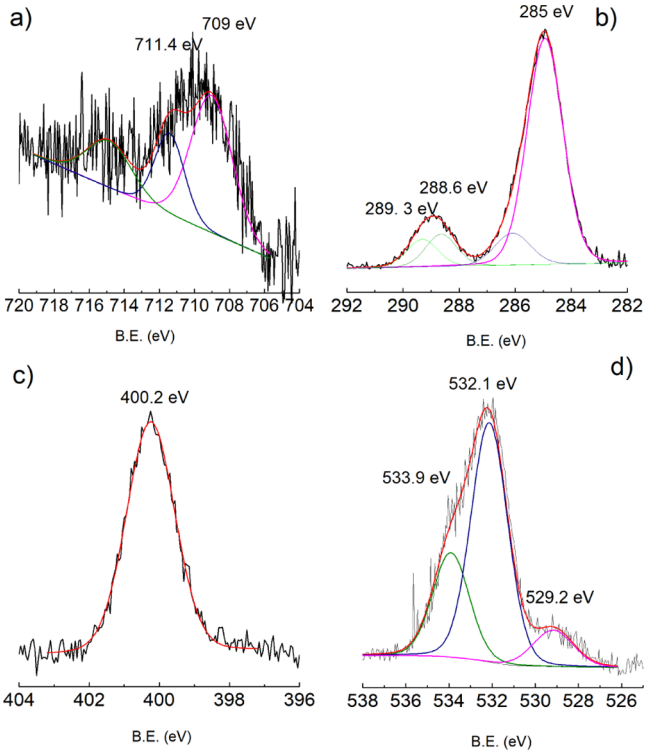

Figure 6. XPS spectra of (a) Fe $2p_{3/2}$, (b) C 1s, (c) N 1s, and (d) O 1s of the α-FeOOH/NH_2-Mil-101 composite.

amorphous FeO.[49] The shape of the C 1s band (Figure 6b) is the result of the contribution of different species. The most intense peak in this region is observed at 285.0 eV, and it is typically associated with aliphatic and aromatic hydrocarbon atoms and to the "adventitious" carbon. The featured peak at 288.9 eV is characteristic of the carboxylic groups. However, the position of this peak is intermediate between the value (289.3 eV) reported for the COOH groups of terephthalic acid[45] and the typical values (288.6–288.2 eV) reported for the carboxylate (COO^-) groups.[45,47] This feature can be, therefore, the result of the contribution of two components at 289.3 and at 288.6 eV due to adsorbed terephthalic acid and the terephthalate ligands of the MOF, respectively. This result is consistent with the FTIR outcomes, which suggests the presence of free terephthalic acid besides the terephthalate ligand of the NH_2-Mil-101 framework. The last component at around 286.1 eV can be associated to the adventitious C–O species and to the C–N atoms of the aminoterephthalic/terephthalate species. As expected, a N 1s signal at 400.2 eV (Figure 6c) is also present because of the aforementioned aminoterephthalic/terephthalate species. The spectrum of O 1s (Figure 6d) shows a main component at 532.1 eV and two shoulders at 529.2 and 533.9 eV. The main component is consistent with the presence of hydroxides and the carboxylate groups of the MOF. The weak signal at low binding energies (529.2 eV) can be assigned to MOs, while the shoulder at 533.9 eV is likely because of adsorbed water.

Electrochemical Behavior of the α-FeOOH/NH_2-Mil-101 Composite. EIS is considered as a powerful tool to get insight into the electrochemical behavior of the MOF-based composite system.[50,51] Figure 7a compares the Nyquist plots (real part vs imaginary part of the impedance) of the bare Cu foil, amorphous sol–gel iron oxides/hydroxides (top inset), and the α-FeOOH/NH_2-Mil-101 composite (bottom inset).

All plots display a semicircular arc in the high frequency region and an almost straight line in the low frequency region. The beginning of the semicircle is the equivalent series resistance (ESR), which represents the combined resistance of the electrolyte, active material/substrate interface, and the substrate. The semicircle is because of the double layer capacitance, described by the constant phase element (CPE) by taking into account the nonideality of the capacitor, in parallel with the charge transfer resistance at the electrolyte/electrode interface (R_{ct}). The straight line is related to the diffusion resistance of the ions within the electrode material and is represented by a Warburg element (CPE with 45° phase) in series with R_{ct}. This peculiar shape can be fitted based on the equivalent circuit model shown in Figure 7b.[52] The resulting fitting parameters are reported in Table 1. Except for the ESR values, the iron oxide/hydroxide film and the α-FeOOH/NH_2-Mil-101 composite present similar circuit parameters, as expected from the very similar impedance curves shown in Figure 7a. In fact, ESR reduces after the sol–gel deposition of the iron oxide/hydroxide film (40 → 22 Ω) and increases after the formation of the hybrid NH_2-Mil-101 structure (22 → 44 Ω) because of the lower conductivity of the MOF. However, the R_{ct} of the iron oxide/hydroxide films

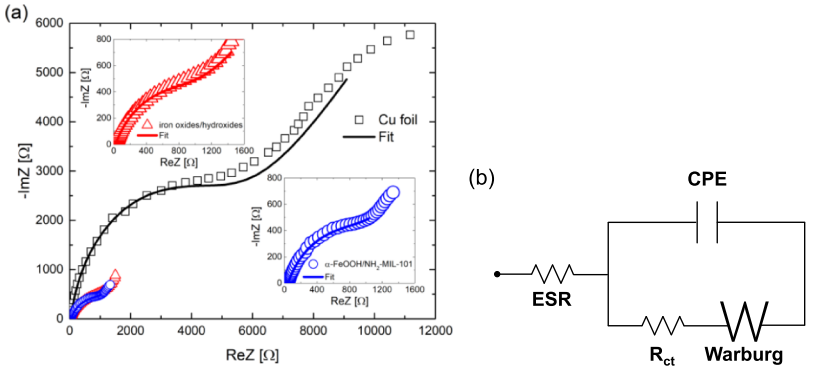

Figure 7. (a) Nyquist plots of the Cu foil (black squares), iron oxides/hydroxides (red triangles), the α-FeOOH/NH_2-Mil-101 composite (blue circles) recorded at 0 V vs open circuit potential with a 10 mV superimposed ac voltage in the frequency range 10^4 to 10^{-1} Hz in 0.1 M KCl electrolytic solution containing 5 mM $[Fe(CN)_6]^{3-/4-}$. The insets are the magnified region of the Nyquist plots of the iron oxide/hydroxide film (top inset) and the α-FeOOH/NH_2-Mil-101 composite (bottom inset) and (b) equivalent circuit model used to fit the Nyquist plots: an ESR is connected in series with a CPE in parallel with the charge transfer resistance (R_{ct}) and a Warburg element (W).

DOI: 10.1021/acsomega.9b01840
ACS Omega 2019, 4, 18495–18501

Table 1. Fitting Parameters Obtained from the Equivalent Circuit Model Reported in Figure 7b

sample	R_{ESR} [Ω]	R_{ct} [Ω]	A_w [Ω $s^{-1/2}$]	CPE [F $s^{(n-1)}$]	n
Cu foil	40 ± 3	5201 ± 354	9012 ± 765	(2.02 ± 0.07) × 10^{-6}	0.885 ± 0.004
iron oxide/hydroxide film	22 ± 1	1157 ± 39	958 ± 57	(6.6 ± 0.1) × 10^{-5}	0.673 ± 0.002
α-FeOOH/NH_2-Mil-101	44 ± 1	1117 ± 73	1087 ± 283	(5.3 ± 0.2) × 10^{-5}	0.663 ± 0.005

and the α-FeOOH/NH_2-Mil-101 samples is almost the same (∼1100 Ω), and it is significantly lower than the one for the Cu foil (∼5000 Ω). Moreover, the CPE values of the iron oxide/hydroxide film and the α-FeOOH/NH_2-Mil-101 are similar (∼50−65 μF $s^{(n-1)}$) and obviously higher than those of the Cu foil (∼2 μF $s^{(n-1)}$) because of their larger surface area. Also, the value of n indicates that the capacitive behavior of the Cu foil (n = 0.885) is close to that of an ideal capacitor (n = 1), while both the iron oxide/hydroxide film and α-FeOOH/NH_2-Mil-101 ($n \approx 0.67$) behave like a nonideal capacitor because of their porous nature. Finally, the value of the Warburg coefficient A_W of the iron oxide/hydroxide film and α-FeOOH/NH_2-Mil-101 suggests an easier diffusion of ions within the electrode. Therefore, the α-FeOOH/NH_2-Mil-101 composite electrode offers the synergistic properties of the two components (α-FeOOH and MOF) without deteriorating the electrochemical features of the classical iron oxide/hydroxide electrodes.

CONCLUSIONS

A novel two-step synthetic strategy was developed to grow Fe-based NH_2-Mil-101 composite films on Cu foil at low temperature (80 °C). An amorphous iron oxide/hydroxide layer deposited via sol−gel was used to provide, directly on a Cu electrode surface, the Fe^{3+} centers needed for the MOF growth. A porous α-FeOOH/NH_2-Mil-101 composite film was then grown using an ethanol solution containing the organic building block only (2-aminoterephthalic acid). The proposed synthetic approach is fast, makes use of mild conditions, and so, it is a convenient protocol to develop hybrid MO/MOF films. EIS measurements have shown that, despite the poor conductivity of the MOF resulting in a high ESR value, both iron oxides/hydroxides and α-FeOOH/NH_2-Mil-101 have similar circuit parameters. In particular, both systems behave like nonideal capacitors with a value of charge transfer resistance of about 1100 Ω, which is lower than that of the Cu benchmark. Despite the insulating character of NH_2-Mil-101, α-FeOOH/NH_2-Mil-101's unique impedance behavior makes it a promising electrode capable of combining the structural and chemicophysical MOF properties with the typical electrochemical characteristics of iron hydroxide materials.

EXPERIMENTAL SECTION

Materials. Iron(III) nitrate nonahydrate, 2-aminoterephthalic acid, ethanol, acetone, isopropanol acetylacetone, methoxyethyelene, potassium chloride, and potassium hexacyanoferrate(III) were purchased from Sigma-Aldrich and used as received.

Sol−Gel Deposition of Amorphous Iron Oxide/Hydroxide Layer. Iron oxide/hydroxide layer was deposited on copper foil through sol−gel deposition using iron(III) nitrate as the precursor and 2-methoxyethanol as the solvent. First, $Fe(NO_3)_3 \times 9H_2O$ was solubilized in a solution of 2-methoxyethanol and acetylacetone in a molar ratio of 10:1. The latter solution (0.2 M) was stirred and kept at room temperature for 2 h. Then, the precursor solution (15 mL) was dropped on the copper foil and cleaned with a mixture of acetone/isopropanol/ethanol in a spin-coater at a spinning rate of 1000−2000 rpm for 30 s. Four spin-coating steps were repeated to increase the layer thickness. In addition, a drying treatment at 100 °C was carried out after each cycle to allow a suitable adhesion on the surface. The sample was, then, annealed at 150 °C (heating rate of 5 °C/min) for 4 h to eliminate the organic components without inducing film crystallization.

Growth of α-FeOOH/NH_2-Mil-101 Films. Composite films were directly grown from solution on the amorphous oxide/hydroxide layer, which act as the source of Fe^{3+} ions. In particular, the samples of iron oxide/hydroxide layer deposited on the Cu foil were dipped into 2-aminoterephthalic acid (0.16 g) and ethanol solution (15 mL). The system was kept under reflux for 4 or 8 h in an 80 °C oil bath. Samples were then washed in ethanol and dried under N_2 flow.

Characterization. FE-SEM (Zeiss Supra35 FE-SEM) was used to observe sample morphology. EDX analyses were performed using an INCA-Oxford windowless detector.

Transmission FTIR measurements were recorded on JASCO FTIR 430, using the KBr pellet technique, with 100 scans collected per spectrum (scan range 560−4000 cm^{-1}, resolution 4 cm^{-1}).

XPS spectra were run using a PHI 5600 multitechnique ESCA-Auger spectrometer equipped with a standard Mg Kα X-ray source. Analyses were carried out with a photoelectron take-off angle of 45° (relative to the sample surface) with an acceptance angle of ±7°. The XPS binding energy scale was calibrated by centering the C 1s peak because of hydrocarbon moieties and "adventitious" carbon at 285.0 eV.

XRD patterns were collected with a D8 Discover (Bruker AXS) diffractometer equipped with a high-precision goniometer (0.0001°), a thin-film attachment (long soller slits), and a Cu Kα source. The acquisitions were done using grazing incidence geometry with an incident angle of 0.4°.

TEM and STEM analyses were done in bright and dark field, respectively. Measurements were performed after scratching the sample on a Cu-lacey-C grid using a JEOL JEM 2010 F microscope operating at 200 kV. EELS analyses were performed using the Gatan Imaging Filter (GIF 2001).

EIS analysis was performed at room temperature by using a VersaSTAT 4 Potentiostat (Princeton Applied Research, USA) and a three-electrode setup with samples (1 cm^2 immersed area) as working electrodes, a Pt wire as the counter electrode, and a saturated calomel electrode. A 0.1 M KCl solution containing 5 mM $[Fe(CN)_6]^{3-/4-}$ was used as the supporting electrolyte. EIS measurements were recorded at 0 V versus open circuit potential with a 10 mV superimposed ac voltage in the frequency range 10^4 to 10^{-1} Hz. EIS spectra were fitted by using EIS spectrum analyser software.

AUTHOR INFORMATION

Corresponding Author

*E-mail: guido.condorelli@unict.it.

DOI: 10.1021/acsomega.9b01840
ACS Omega 2019, 4, 18495−18501

ORCID

Mario Urso: 0000-0001-7993-8138
Alessandra Alberti: 0000-0002-4103-6208
Salvo Mirabella: 0000-0002-9559-4862
Guglielmo Guido Condorelli: 0000-0001-6106-8875

Author Contributions

The manuscript was written through contributions of all authors. All authors have given approval to the final version of the manuscript.

Notes

The authors declare no competing financial interest.

■ ACKNOWLEDGMENTS

Authors thank the University of Catania for the project "Piano della Ricerca di Ateneo 2016−2018".

■ REFERENCES

(1) Xu, Y.; Li, Q.; Xue, H.; Pang, H. Metal-Organic Frameworks for Direct Electrochemical Applications. *Coord. Chem. Rev.* **2018**, *376*, 292−318.

(2) Patwardhan, S.; Schatz, G. C. Theoretical Investigation of Charge Transfer in Metal Organic Frameworks for Electrochemical Device Applications. *J. Phys. Chem. C* **2015**, *119*, 24238−24247.

(3) Xue, Y.; Zheng, S.; Xue, H.; Pang, H. Metal-Organic Framework Composites and Their Electrochemical Applications. *J. Mater. Chem. A* **2019**, *7*, 7301.

(4) Sundriyal, S.; Kaur, H.; Bhardwaj, S. K.; Mishra, S.; Kim, K.-H.; Deep, A. Metal-Organic Frameworks and Their Composites as Efficient Electrodes for Supercapacitor Applications. *Coord. Chem. Rev.* **2018**, *369*, 15−38.

(5) Denny, M. S.; Kalaj, M.; Bentz, K. C.; Cohen, S. M. Multicomponent Metal-Organic Framework Membranes for Advanced Functional Composites. *Chem. Sci.* **2018**, *9*, 8842−8849.

(6) Oar-Arteta, L.; Wezendonk, T.; Sun, X.; Kapteijn, F.; Gascon, J. Metal Organic Frameworks as Precursors for the Manufacture of Advanced Catalytic Materials. *Mater. Chem. Front.* **2017**, *1*, 1709−1745.

(7) Li, C.; Hu, Q.; Li, Y.; Zhou, H.; Lv, Z.; Yang, X.; Liu, L.; Guo, H. Hierarchical Hollow Fe2O3 @MIL-101(Fe)/C Derived from Metal-Organic Frameworks for Superior Sodium Storage. *Sci. Rep.* **2016**, *6*, 25556.

(8) Farisabadi, A.; Moradi, M.; Hajati, S.; Kiani, M. A.; Espinos, J. P. Controlled Thermolysis of MIL-101(Fe, Cr) for Synthesis of Fe X O Y /porous Carbon as Negative Electrode and Cr 2 O 3 /porous Carbon as Positive Electrode of Supercapacitor. *Appl. Surf. Sci.* **2019**, *469*, 192−203.

(9) Cardenas-Morcoso, D.; Ifraemov, R.; García-Tecedor, M.; Liberman, I.; Gimenez, S.; Hod, I. A Metal-Organic Framework Converted Catalyst That Boosts Photo-Electrochemical Water Splitting. *J. Mater. Chem. A* **2019**, *7*, 11143−11149.

(10) Zhou, J.; Dou, Y.; Zhou, A.; Shu, L.; Chen, Y.; Li, J.-R. Layered Metal-Organic Framework-Derived Metal Oxide/Carbon Nanosheet Arrays for Catalyzing the Oxygen Evolution Reaction. *ACS Energy Lett.* **2018**, *3*, 1655−1661.

(11) Chae, H. K.; Siberio-Perez, D. Y.; Kim, J.; Go, Y.; Eddaoudi, M.; Matzger, A. J.; O'Keeffe, M.; Yaghi, O. M. A route to high surface area, porosity and inclusion of large molecules in crystals. *Nature* **2004**, *427*, 523−527.

(12) Davis, M. E. Ordered Porous Materials for Emerging Applications. *Nature* **2002**, *417*, 813−821.

(13) Zhang, W.-X.; Liao, P.-Q.; Lin, R.-B.; Wei, Y.-S.; Zeng, M.-H.; Chen, X.-M. Metal Cluster-Based Functional Porous Coordination Polymers. *Coord. Chem. Rev.* **2015**, *293−294*, 263−278.

(14) Cui, Y.; Li, B.; He, H.; Zhou, W.; Chen, B.; Qian, G. Metal-Organic Frameworks as Platforms for Functional Materials. *Acc. Chem. Res.* **2016**, *49*, 483−493.

(15) Tanabe, K. K.; Cohen, S. M. Postsynthetic Modification of Metal−organic Frameworks—a Progress Report. *Chem. Soc. Rev.* **2011**, *40*, 498−519.

(16) Campbell, M. G.; Dincă, M. Metal−organic Frameworks as Active Materials in Electronic Sensor Devices. *Sensors* **2017**, *17*, 1108.

(17) Oar-Arteta, L.; Wezendonk, T.; Sun, X.; Kapteijn, F.; Gascon, J. Metal Organic Frameworks as Precursors for the Manufacture of Advanced Catalytic Materials. *Mater. Chem. Front.* **2017**, *1*, 1709−1745.

(18) Pastore, V. J.; Cook, T. R.; Rzayev, J. Polymer-MOF Hybrid Composites with High Porosity and Stability through Surface-Selective Ligand Exchange. *Chem. Mater.* **2018**, *30*, 8639.

(19) Li, Y.; Xu, Y.; Yang, W.; Shen, W.; Xue, H.; Pang, H. MOF-Derived Metal Oxide Composites for Advanced Electrochemical Energy Storage. *Small* **2018**, *14*, 1704435.

(20) Martinet, S. *Nanomaterials for Rechargeable Lithium Batteries*; Springer, 2016; pp 471−512.

(21) Wu, H. B.; Chen, J. S.; Hng, H. H.; Wen Lou, X. Nanostructured Metal Oxide-Based Materials as Advanced Anodes for Lithium-Ion Batteries. *Nanoscale* **2012**, *4*, 2526−2542.

(22) Kim, U.-H.; Jun, D.-W.; Park, K.-J.; Zhang, Q.; Kaghazchi, P.; Aurbach, D.; Major, D. T.; Goobes, G.; Dixit, M.; Leifer, N.; et al. Pushing the Limit of Layered Transition Metal Oxide Cathodes for High-Energy Density Rechargeable Li Ion Batteries. *Energy Environ. Sci.* **2018**, *11*, 1271−1279.

(23) Zhang, E.; Wang, B.; Yu, X.; Zhu, J.; Wang, L.; Lu, B. *β*-FeOOH on Carbon Nanotubes as a Cathode Material for Na-Ion Batteries. *Energy Storage Mater.* **2017**, *8*, 147−152.

(24) Wu, Z.-S.; Zhou, G.; Yin, L.-C.; Ren, W.; Li, F.; Cheng, H.-M. Graphene/metal Oxide Composite Electrode Materials for Energy Storage. *Nano Energy* **2012**, *1*, 107−131.

(25) Yu, L.; Wang, L. P.; Xi, S.; Yang, P.; Du, Y.; Srinivasan, M.; Xu, Z. J. *β*-FeOOH: An Earth-Abundant High-Capacity Negative Electrode Material for Sodium-Ion Batteries. *Chem. Mater.* **2015**, *27*, 5340−5348.

(26) Gao, M.; Zhou, P.; Wang, P.; Wang, J.; Liang, C.; Zhang, J.; Liu, Y. FeO/C Anode Materials of High Capacity and Cycle Stability for Lithium-Ion Batteries Synthesized by Carbothermal Reduction. *J. Alloys Compd.* **2013**, *565*, 97−103.

(27) Zhuang, L. Low-Crystalline Iron Oxide Hydroxide Nanoparticles: High-Performance Anode for Supercapacitors. *Acta Phys.-Chim. Sin.* **2017**, *33*, 859−860.

(28) Pervez, S. A.; Kim, D.; Farooq, U.; Yaqub, A.; Choi, J.-H.; Lee, Y.-J.; Muhammad, S.; Doh, C.-H. Crystalline Iron Oxide Nanotube Arrays with High Aspect Ratio as Binder Free Anode for Li-Ion Batteries. *Phys. Status Solidi A* **2014**, *211*, 1889−1894.

(29) Tian, B.; Świątowska, J.; Maurice, V.; Pereira-Nabais, C.; Seyeux, A.; Marcus, P. Insight into Lithium Diffusion in Conversion-Type Iron Oxide Negative Electrode. *J. Phys. Chem. C* **2015**, *119*, 919−925.

(30) Zhu, C.; Saito, G.; Akiyama, T. A Facile Solution Combustion Synthesis of Nanosized Amorphous Iron Oxide Incorporated in a Carbon Matrix for Use as a High-Performance Lithium Ion Battery Anode Material. *J. Alloys Compd.* **2015**, *633*, 424−429.

(31) Li, D.; Zhou, J.; Chen, X.; Song, H. Amorphous Fe2O3/Graphene Composite Nanosheets with Enhanced Electrochemical Performance for Sodium-Ion Battery. *ACS Appl. Mater. Interfaces* **2016**, *8*, 30899−30907.

(32) Amine, K.; Yasuda, H.; Yamachi, M. *β*-FeOOH, a new positive electrode material for lithium secondary batteries. *J. Power Sources* **1999**, *81−82*, 221−223.

(33) Abdel-Samad, H.; Watson, P. R. An XPS Study of the Adsorption of Chromate on Goethite (*α*-FeOOH). *Appl. Surf. Sci.* **1997**, *108*, 371−377.

(34) Wezendonk, T. A.; Santos, V. P.; Nasalevich, M. A.; Warringa, Q. S. E.; Dugulan, A. I.; Chojecki, A.; Koeken, A. C. J.; Ruitenbeek, M.; Meima, G.; Islam, H.-U.; et al. Elucidating the Nature of Fe Species during Pyrolysis of the Fe-BTC MOF into Highly Active and Stable Fischer-Tropsch Catalysts. *ACS Catal.* **2016**, *6*, 3236−3247.

DOI: 10.1021/acsomega.9b01840
ACS Omega 2019, 4, 18495−18501

(35) Xu, X.; Cao, R.; Jeong, S.; Cho, J. Spindle-like Mesoporous α-Fe2O3 Anode Material Prepared from MOF Template for High-Rate Lithium Batteries. *Nano Lett.* **2012**, *12*, 4988−4991.
(36) Li, C.; Hu, Q.; Li, Y.; Zhou, H.; Lv, Z.; Yang, X.; Liu, L.; Guo, H. Hierarchical Hollow Fe2O3 @MIL-101(Fe)/C Derived from Metal-Organic Frameworks for Superior Sodium Storage. *Sci. Rep.* **2016**, *6*, 25556.
(37) Li, Y.; Xu, Y.; Yang, W.; Shen, W.; Xue, H.; Pang, H. MOF-Derived Metal Oxide Composites for Advanced Electrochemical Energy Storage. *Small* **2018**, *14*, 1704435.
(38) Bétard, A.; Fischer, R. A. Metal-Organic Framework Thin Films : From Fundamentals To Applications. *Chem. Rev.* **2012**, *112*, 1055−1083.
(39) Monforte, F.; Mannino, G.; Alberti, A.; Smecca, E.; Italia, M.; Motta, A.; Tudisco, C.; Condorelli, G. G. Heterogeneous Growth of Continuous ZIF-8 Films on Low-Temperature Amorphous Silicon. *Appl. Surf. Sci.* **2019**, *473*, 182−189.
(40) Yin, D.; Li, C.; Ren, H.; Shekhah, O.; Liu, J.; Liang, C. Efficient Pd@MIL-101(Cr) Hetero-Catalysts for 2-Butyne-1,4-Diol Hydrogenation Exhibiting High Selectivity. *RSC Adv.* **2017**, *7*, 1626−1633.
(41) Xie, Q.; Li, Y.; Lv, Z.; Zhou, H.; Yang, X.; Chen, J.; Guo, H. Effective Adsorption and Removal of Phosphate from Acqueous Solution and Euthrophic Water by Fe-based MOfs of MIL-1101. *Sci. Rep.* **2017**, *7*, 3316.
(42) Ghosh, M. K.; Poinern, G. E. J.; Issa, T. B.; Singh, P. Arsenic Adsorption on Goethite Nanoparticles Produced through Hydrazine Sulfate Assisted Synthesis Method. *Korean J. Chem. Eng.* **2012**, *29*, 95−102.
(43) Stoia, M.; Istratie, R.; Păcurariu, C. Investigation of Magnetite Nanoparticles Stability in Air by Thermal Analysis and FTIR Spectroscopy. *J. Therm. Anal. Calorim.* **2016**, *125*, 1185−1198.
(44) Sharma, G.; Jeevanandam, P. Synthesis of Self-Assembled Prismatic Iron Oxide Nanoparticles by a Novel Thermal Decomposition Route. *RSC Adv.* **2013**, *3*, 189−200.
(45) Tudisco, C.; Pellegrino, A. L.; Malandrino, G.; Condorelli, G. G. Surface Anchoring of Bi-Functional Organic Linkers on Piezoelectric $BiFeO_3$ Films and Particles: Comparison between Carboxylic and Phosphonic Tethering Groups. *Surf. Coat. Technol.* **2018**, *343*, 75−82.
(46) Sun, J.; Yu, G.; Huo, Q.; Kan, Q.; Guan, J. Epoxidation of Styrene over Fe(Cr)-MIL-101 Metal−organic Frmeworks. *RSC Adv.* **2014**, *4*, 38048−38054.
(47) Liang, R.; Jing, F.; Shen, L.; Qin, N.; Wu, L. MIL-53(Fe) as a Highly Efficient Bifunctional Photocatalyst for the Simultaneous Reduction of Cr(VI) and Oxidation of Dyes. *J. Hazard. Mater.* **2015**, *287*, 364−372.
(48) Gao, C.; Chen, S.; Quan, X.; Yu, H.; Zhang, Y. Enhanced Fenton-like Catalysis by Iron-Based Metal Organic Frameworks for Degradation of Organic Pollutants. *J. Catal.* **2017**, *356*, 125−132.
(49) Luo, H.; Su, H.; Dong, C.; Li, X. Passivation and Electrochemical Behavior of 316L Stainless Steel in Chlorinated Simulated Concrete Pore Solution. *Appl. Surf. Sci.* **2017**, *400*, 38−48.
(50) Zhang, Y.; Bo, X.; Luhana, C.; Wang, H.; Li, M.; Guo, L. Facile Synthesis of a Cu-Based MOF Confined in Macroporous Carbon Hybrid Material with Enhanced Electrocatalytic Ability. *Chem. Commun.* **2013**, *49*, 6885−6887.
(51) Yang, J.; Zhao, F.; Zeng, B. One-Step Synthesis of a Copper-Based Metal-Organic Framework-Graphene Nanocomposite with Enhanced Electrocatalytic Activity. *RSC Adv.* **2015**, *5*, 22060−22065.
(52) Urso, M.; Torrisi, G.; Boninelli, S.; Bongiorno, C.; Priolo, F.; Mirabella, S. Ni(OH)2@Ni Core-Shell Nanochains as Low-Cost High-Rate Performance Electrode for Energy Storage Applications. *Sci. Rep.* **2019**, *9*, 7736.

DOI: 10.1021/acsomega.9b01840
ACS Omega 2019, 4, 18495−18501